

Multiscale mechanics of thermal gradient coupled graphene fracture: A molecular dynamics study

Hanfeng Zhai^{a)}

Sibley School of Mechanical and Aerospace Engineering
Cornell University

(Dated: 15 August 2022)

Synopsis

The thermo-mechanical coupling mechanism of graphene fracture under thermal gradients possesses rich applications whereas hard to study due to its coupled non-equilibrium nature. We employ non-equilibrium molecular dynamics to study the fracture of graphene by applying a fixed strain rate under different thermal gradients by employing different potential fields. It is found that for AIREBO and AIREBO-M the fracture stresses do not strictly follow the positive correlations with the initial crack length. Strain-hardening effects are observed for “REBO-based” potential models of small initial defects, which is interpreted as blunting effect observed for porous graphene. The temperature gradients are observed to not show clear relations with the fracture stresses and crack propagation dynamics. Quantized fracture mechanics verifies our molecular dynamics calculations. We provide a unique perspective that the transverse bond forces share the loading to account for the nonlinear increase of fracture stress with shorter crack length. Anomalous kinetic energy transportation along crack tips is observed for “REBO-based” potential models, which we attribute to the high interatomic attractions in the potential models. The fractures are honored to be more “brittle-like” carried out using machine learning interatomic potential (MLIP), yet incapable of simulating post fracture dynamical behaviors. The mechanical responses using MLIP are observed to be not related to temperature gradients. The temperature configuration of equilibration simulation employing the dropout uncertainty neural network potential with a dropout rate of 0.2 is reported to be the most accurate compared with the rest. This work is expected to inspire further investigation of non-equilibrium dynamics in graphene with practical applications in various engineering fields.

Novelty Statement

- non-equilibrium molecular dynamics were employed to study graphene fracture under temperature gradients with fixed strain rate, where the effect of initial defect sizes, temperature differences, and potential fields are investigated.
- The stress-strain responses are highly dependent on potentials, where the fracture stresses don't positively correlate with initial defect sizes for “REBO-based” potentials, with strain-hardening effects observed.
- The fracture direction is reported to be not related to temperature gradients.
- An abnormal fracture form is observed for “REBO-based” potentials, where the kinetic energy is transported along with the crack tips before fracture and is more frequently observed for longer initial pores of higher temperature differences.
- A comparative study of empirical MD potentials with state-of-the-art *ab initio*-based machine learning potentials is also presented, where the limitations and the fracture characterizations are elaborated.

Keywords Two-dimensional materials; nanomaterials; molecular dynamics; fracture; heat transfer; machine learning potentials

^{a)}Electronic mail: hz253@cornell.edu; The main manuscript is still in revision by Prof. Jingjie Yeo, and this is an unrevised version.

I. INTRODUCTION

Two-dimensional materials is one of the fastest growing and active nanomaterials research areas, due to its exceptional mechanical (Liu and Wu, 2016; Akinwande *et al.*, 2017; Wei and Yang, 2018), thermal (Kasirga, 2020; Song *et al.*, 2018; Gu *et al.*, 2018), electrical properties (Bunch, 2008; Ando, 2009). Graphene is a 2D material with a single layer of carbon atoms arranged in a honeycomb lattice structure with sp^2 bonds (Ng, Yeo, and Liu, 2012). The successful synthesis of graphene (Novoselov *et al.*, 2004) has lead to a drastic growing technological advancement based on graphene innovation in semiconductor (Obeng and Srinivasan, 2011; Xie *et al.*, 2018), battery (Wang *et al.*, 2009; Chen *et al.*, 2017), biomedical devices (Yang *et al.*, 2013; Shareena *et al.*, 2018), water desalination (Boretti *et al.*, 2018; Homaeigohar and Elbahri, 2017), and various industrial applications, largely thanks to its superior mechanical (Xu and Buehler, 2009; Xu *et al.*, 2012) and thermal properties (Balandin *et al.*, 2008; Hu, Ruan, and Chen, 2009; Balandin, 2011).

More specifically, the high toughness (Zhang, Li, and Gao, 2015; Xu *et al.*, 2012; Yanovsky *et al.*, 2009), strength (Papageorgiou, Kinloch, and Young, 2017; Wan *et al.*, 2021), and thermal conductivity (Ng, Yeo, and Liu, 2012; Jung *et al.*, 2017) makes graphene an ideal candidate for various engineering applications. Fracture is one of the most prominent concerns for graphene (Zhang, Li, and Gao, 2015), in which the nonlinear elastic regime plays a significant role in determining graphene strength (Wei and Kysar, 2012; Lee *et al.*, 2008). Both strength and defects majorly contribute to graphene fracture (Wei and Yang, 2018). Topological defects like dislocations and grain boundaries can alter both mechanical (Grantab, Shenoy, and Ruoff, 2010; Wei *et al.*, 2012; Zhang, Zhao, and Lu, 2012) and thermal properties (Ng, Yeo, and Liu, 2012; Wei and Yang, 2018; Bagri *et al.*, 2011; Li *et al.*, 2019) of graphene. The thermo-mechanical coupling mechanism effects of graphene fracture remain an interesting and ongoing topic. Jangid and Kottantharayil (Jangid and Kottantharayil, 2020) show that methane gas treatment at a high temperature can reconstruct fractured graphene, considering electrical breakdown due to resistive heating is one of the main reasons for graphene fracture. Liu et al. (Liu *et al.*, 2020) tailor the microstructure of graphene composite to enable both high thermal conductivity and toughness. Most interestingly, Yo, Xu and Ding (Yoo, Xu, and Ding, 2021) use both experimental and Monte Carlo simulations to show that under high-temperature heat treatment multiple single-wall carbon nanotubes (SWCNT) merge into new morphology, as temperature difference may elicit carbon-carbon bond breaks and reform SWCNT.

The development of machine learning and data-driven methods advances new techniques in computational modeling and molecular simulations. One such example is the machine learning potential (MLP). Most MLPs adopt the pioneering ideology by Behler and coworkers (Behler and Parrinello, 2007; Artrith, Morawietz, and Behler, 2011; Artrith and Behler, 2012) of utilizing neural networks to learn the molecular energy configuration based on first principle calculations to scale up *ab initio* calculations. E and coworkers developed deep potential molecular dynamics (DeePMD) that can adjust to different atomic configurations in 2018 (Wang *et al.*, 2018; Zhang *et al.*, 2018). Shapeev and coworkers developed machine learning interatomic potentials (MLIP) based on moment tensor operations in 2021 (Novikov *et al.*, 2021). Wen et al. elicit dropout matrices to thin the original neural networks for less uncertainty called dropout uncertainty neural network (DUNN) in 2020 (Wen and Tadmor, 2020). For the ease of fast implementation in PyTorch, Gao et al. developed a framework called TorchANI (Gao *et al.*, 2020). Most recently, Jung et al. (Jung, Myung, and Irle, 2022) develop a machine learning potential using TorchANI specifically for graphene fracture. In training the machine learning potentials, Jung et al. (Jung, Myung, and Irle, 2022) and DUNN (Wen and Tadmor, 2020, 2019) formulations include the differences of energy and forces in the loss function, whereas the MLIP (Novikov *et al.*, 2021) and DeePMD (Wang *et al.*, 2018) also include the (virial) stress. With all these great milestones, we are essentially curious about how will these MLPs compare with empirical potentials in molecular simulations.

Inspired by the work of Yo, Xu, and Ding (Yoo, Xu, and Ding, 2021) and Jangid and

Kottantharayil (Jangid and Kottantharayil, 2020), an interesting question hence arises, how may heat work during the graphene fracture process? This question is significant in three aspects, (1) Theoretically, the fracture process under heat gradient is nonlinear and non-equilibrium in nature (Yuan and Kalkhof, 2000), which is hard to either model or experiment. Hence, describing the physical details is difficult, which will be elaborated on in the next paragraph. (2) Consider the prementioned wide applications, graphene layer(s) under thermal gradient is an omnipresent scenario, either as materials for battery or semiconductor (Wang *et al.*, 2009; Chen *et al.*, 2017; Obeng and Srinivasan, 2011; Xie *et al.*, 2018), and in which defects are somehow unavoidable (Wei and Yang, 2018; Araujo, Terrones, and Dresselhaus, 2012; Hashimoto *et al.*, 2004). Therefore, solving this problem has valuable industrial potential. (3) There are few related works that exist. As mentioned, there do exist numerous works that either study the graphene mechanical (Hu *et al.*, 2021; Xu and Buehler, 2009) or thermal properties (Balandin *et al.*, 2008; Hu, Ruan, and Chen, 2009; Balandin, 2011) either separately or measure related parameters under equilibrium state (Xu *et al.*, 2012; Hu *et al.*, 2021; Felix *et al.*, 2020), creating a vacant space for non-equilibrium thermo-mechanical coupling study of graphene fracture.

In theory, changing the graphene temperature transduces a thermal gradient between the heat source and sink, during which the physical system is in non-equilibrium (Yuan and Kalkhof, 2000). At the molecular scale, the fracture of graphene is fundamentally the breaking of carbon-carbon bonds, which in essence is also a non-equilibrium process. Interested in the mechanism behind such processes, we employ non-equilibrium molecular dynamics simulations (NEMD) to study the fracture behavior of a single graphene layer under thermal gradients. We adopt four of the most commonly used empirical potentials, reactive bond order (REBO) (Brenner *et al.*, 2002), adaptive intermolecular REBO (AIREBO) (Stuart, Tutein, and Harrison, 2000), AIREBO-M (O'Connor, Andzelm, and Robbins, 2015), and optimized Tersoff (Lindsay and Broido, 2010), and study the graphene thermo-mechanical responses for fracture characterization. We also adopt the MLIP (Novikov *et al.*, 2021) and DUNN (Wen and Tadmor, 2020) to characterize the difference within MLPs and compared them with empirical potentials.

The manuscript is arranged as follows: in Section II we briefly introduce the mathematical derivation of the empirical potentials (Sec. II A) and machine learning potentials (Sec. II B); our numerical setup, including problem formulation with the simulation details. The results are presented and discussed in Section III, where effect of the empirical potentials are elaborated in Sec. III A, the thermo-mechanical mechanism under the fracture process are proposed in Sec. III B, the fracture dynamics are characterized in Sec. III C and the comparison with machine learning potentials are proposed in Sec. II B. Eventually, we conclude the paper in Section IV.

II. METHODOLOGY AND MODELING

A. Empirical Interatomic Potentials

In molecular modeling of materials, interatomic potentials constitute the materials' overall physical properties. Empirical potentials describing the atomic interactions are proposed utilizing symbolic form with fitted parameters to calculate the energy and potential spaces with interatomic motion based on Newtonian dynamics. Here, several widely applied empirical potentials are adopted for graphene in our modeling.

Generally, the atomic energies can be expanded in series as the sum of potentials, in which similar models can be viewed as an analog of Taylor series expansion. Based on these ideas, the energy of N interacting particles can be written as:

$$E = \sum_i V_i(\mathbf{r}_i) + \sum_{i < j} V_2(\mathbf{r}_i, \mathbf{r}_j) + \sum_{i < j < k} V_3(\mathbf{r}_i, \mathbf{r}_j, \mathbf{r}_k) + \dots, \quad (1)$$

where \mathbf{r}_n is the position of the n^{th} particle, and V_m is called the m -body potential, where

$\sum_i V_i(\mathbf{r}_i)$ is the external potential. Details elaborations could be found in Ref. (Tersoff, 1988). Most empirical potentials only consider the first term as a description of the particles' interactions in the two-body term. Here, we briefly elaborate on the basic form of interatomic potentials V_{ij} and energies E for different models for further physical explanations.

1. Optimized Tersoff

In the Tersoff proposition, (Tersoff, 1986, 1988), the potential was fitted to guarantee the universal behavior of calculated energy curves can be mapped to a single-dimensionless curve through parameterized rescaling, as shown by Ferrante, Smith, and Rose (Ferrante, Smith, and Rose, 1983; Rose, Smith, and Ferrante, 1983). Such an interatomic potential is taken to have the form:

$$\begin{aligned} E^{\text{Tersoff}} &= \sum_i E_i^{\text{Tersoff}} = \frac{1}{2} \sum_{i \neq j} V_{ij}^{\text{Tersoff}}, \\ V_{ij}^{\text{Tersoff}} &= f_C^{\text{Tersoff}}(r_{ij}) \left[A e^{(-\lambda_1 r_{ij})} - B_{ij} e^{(-\lambda_2 r_{ij})} \right] \end{aligned} \quad (2)$$

where E is the total energy of the system, E_i is site i 's site energy, to make the asymmetry of V_{ij} more intuitive. V_{ij} and r_{ij} are the interaction energy and distance between atom i and j ; and both A , B , λ_1 and λ_2 are parameters with positive values, with $\lambda_1 > \lambda_2$. f_c is the cutoff function to restrict potential ranges. The second term of V_{ij} represents bonding, where B_{ij} hence includes bond order and depends upon the environment. The detailed form of the parameters A , B_{ij} , λ , ..., are given in the Electronic Supplementary Information (ESI) and Ref (Tersoff, 1986).

In 2010, Lindsay and Broido (Lindsay and Broido, 2010) proposed an optimized version of Tersoff potential, which was later proven to have much better accuracy in describing the graphene's thermal properties compared with the original Tersoff, REBO, and AIREBO potentials (Si *et al.*, 2017). In the optimized form, the well-known chi-square minimization was performed to optimize the targeted parameters (Lindsay and Broido, 2010; Mahdizadeh and Akhlagamadi, 2017). The chi-square (χ^2) is given by

$$\chi^2 = \sum_i \frac{\mathcal{U}_i - \mathcal{U}_{\mathbb{B}}}{\mathcal{U}_{\mathbb{B}}^2} \zeta_i \quad (3)$$

where $\mathcal{U}_{\mathbb{B}}$ are benchmark parameters used in the fitting process, which can be based on first-principal calculation (Mahdizadeh and Akhlagamadi, 2017), experiments (Lindsay and Broido, 2010), etc. \mathcal{U}_i are the corresponding values obtained from the original Tersoff potential, and ζ_i are weighting factors determines the relative importance of \mathcal{U}_i in the fitting process. In our approach, the fitted parameters for the optimized Tersoff potential are given in ESI.

2. Reactive Bond Order (REBO)

The reactive bond order (REBO) potential is first proposed by Brenner (Brenner, 1990, 1992), which is an exclusively short-ranged potential (Stuart, Tutein, and Harrison, 2000). The interaction of two atoms is computed only when their distance is less than a covalent-bonding cutoff r_{ij}^{\max} , where the interaction follows:

$$E_{ij}^{\text{REBO}} = \sum_{j \neq i} f_c^{\text{REBO}}(r_{ij}) [V_R(r_{ij}) + \bar{b}_{ij} V_{ij}^A] \quad (4)$$

where V_{ij}^R and V_{ij}^A are the repulsive and attractive pairwise potentials between atoms i and j determined through their distance r_{ij} . \bar{b}_{ij} is the many-body term (see ESI). The repulsive

V^R and attractive V^A terms takes the form (Brenner, 1990):

$$\begin{aligned} V_{ij}^R &= \sum_{n=1}^3 B_n e^{\beta_n r} \\ V_{ij}^A &= \left(1 + \frac{Q}{r}\right) A e^{\alpha r} \end{aligned} \quad (5)$$

where A , B_n , β_n , α , ..., are given in the ESI. Note that V_{ij}^A is switched off for nonshort-ranged atomic interactions through bond weights. More details can also be found in Refs (Stuart, Tutein, and Harrison, 2000; Brenner, 1992, 1990).

3. Adaptive Intermolecular REBO (AIREBO)

Successful in describing intramolecular interactions, REBO potential still suffers from the lack of inclusion of the intermolecular interactions. Stuart et al. (Stuart, Tutein, and Harrison, 2000) further proposed the adaptive intermolecular REBO (AIREBO) method, adding Leonard-Jones (LJ) and torsional interactions to the total potential:

$$E^{\text{AIREBO}} = \frac{1}{2} \sum_i \sum_{j \neq i} \left[E_{ij}^{\text{REBO}} + E_{ij}^{\text{LJ}} + \sum_{k \neq i, j} \sum_{l \neq i, j, k} E_{kijl}^{\text{TORSION}} \right] \quad (6)$$

where the detailed form of E_{ij}^{LJ} and $E_{kijl}^{\text{TORSION}}$ and their corresponding $V_{ij}^{\text{LJ}}(r_{ij})$ and $V_{kijl}^{\text{TORSION}}(r_{ij})$ are given in the ESI. Detailed derivation can be found in Ref (Stuart, Tutein, and Harrison, 2000).

4. AIREBO-M

Even with the added intermolecular terms, the AIREBO potential still has the drawback of inaccurate modeling of high-pressure systems, caused by its high repulsive forces. Further, O'Connor, Andzelm, and Robbins (O'Connor, Andzelm, and Robbins, 2015) replaced the LJ interactions with the Morse potential to more accurately describe the intermolecular interactions:

$$V_{ij}^{\text{MORSE}}(r) = -\epsilon_{ij} \left[1 - \left(1 - e^{\alpha_{ij}(r - r_{ij}^{eq})} \right)^2 \right] \quad (7)$$

where the depth and location of the minimum energy is defined through ϵ and r^{eq} . α modifies the curvature of the potential energy.

The total energy and the potential energy can then be obtained via solving the Schrödinger Equation (David, 2003)

$$-\frac{\hbar}{2m} \frac{d^2\psi}{dx^2} + V^{\text{MORSE}}\psi = E^{\text{MORSE}}\psi \quad (8)$$

where ψ is the wave function, \hbar is the Planck constant, and m is the particle's mass.

Hence, the final form of the total energy of AIREBO-M potential is:

$$E^{\text{AIREBO-M}} = E^{\text{REBO}} + E^{\text{MORSE}} + E^{\text{TORSION}} \quad (9)$$

where detailed parameterization and definition of the Morse potential can be found in the ESI and Ref (O'Connor, Andzelm, and Robbins, 2015).

Here, the introduced four empirical potentials were employed in modeling the nanoporous graphene fracture under thermal gradients with high strain rate loading for comparison and unveiling the underlying mechanism and the physics.

B. Machine Learning *ab initio* Potentials

The core idea of machine learning potentials (MLP) is to employ machine learning (neural networks in our cases) as an approximator to scale up molecular interactions based on quantum-mechanical calculations. Most state-of-the-art MLP models follow the pioneering work conducted by Behler and coworkers (Behler and Parrinello, 2007; Artrith, Morawietz, and Behler, 2011; Artrith and Behler, 2012), which construct the *ab initio* computational domain via atomic configuration as input for the machine learning model to construct the surrogates with energy fields as output. The general supervised learning task is formulated and the approximator (i.e., neural networks, Gaussian process) is trained on data based on density functional theory (DFT), *ab initio* molecular dynamics (AIMD) or other first principle methods. The learned energy fields can then be extended to calculate the interactions at the molecular level based on Newtonian dynamics. Here, two widely used MLP, MLIP (Novikov *et al.*, 2021) and DUNN (Wen and Tadmor, 2020), are adopted to benchmark the calculation of graphene properties.

1. Machine-Learning Interatomic Potentials (MLIP)

The MLIP model was first proposed by Sahpeev and coworkers (Novikov *et al.*, 2021, 2022) and later implemented in graphene (Mortazavi *et al.*, 2022, 2021). They apply moment tensor potentials (MTP) to seamlessly accelerate first principle calculations and incorporate active learning strategies for more efficient training and model construction. The total energy takes the form,

$$E^{\text{MTP}} = \sum_{i=1}^n V_i(\mathbf{r}_i) \longrightarrow V_i(\mathbf{r}_i) = \sum_{\alpha} \xi_{\alpha} B_{\alpha}(\mathbf{r}_i) \quad (10)$$

Here, the function V is linearly expanded through a set of basis function B_{α} . $\xi = \{\xi_{\alpha}\}$ are parameters obtained through fitting to the training sets. Sahpeev and coworkers then introduce moment tensor descriptors and construct the basis functions from the level of these moments. More details can be found in the ESI and their tutorial paper (Novikov *et al.*, 2021).

Suppose the quantum-mechanical energy E^{QM} are known for training, with their corresponding stress tensors σ^{QM} . The whole learning process can be viewed as using NN as an approximator to fit the known energy and stresses. If we denote the fitting parameters as θ , the fitting procedure can be simplified as:

$$\mathcal{L} = \sum_{k=1}^K \left[w_e \mathcal{E}(E^{\text{MTP}}, E^{\text{QM}}) + w_f \sum_{i=1}^{N_k} \mathcal{E}(\mathbf{f}_i^{\text{MTP}}, \mathbf{f}_i^{\text{QM}}) + w_s \mathcal{E}(\sigma^{\text{MTP}}, \sigma^{\text{QM}}) \right] \rightarrow \min_{\theta} \quad (11)$$

where N_k is the atomic numbers in the k^{th} configuration. w_e , w_f , and w_s are weights for energies, forces and stresses. \mathcal{E} is the error measurements, i.e., mean-square errors (MSE), root MSE, and absolute errors. \mathcal{L} is the loss function subjected to be minimized during the optimization process. θ are the hyperparameters contained in the MTP predicted physical properties evolving during the optimization process. The detailed forms are given in the ESI and further derivation in Ref (Novikov *et al.*, 2021). Here, MLIP is used to replace traditional empirical potentials to benchmark the simulations of the extreme porous graphene fracture.

2. Dropout Uncertainty Neural Network (DUNN)

Even though MLP methods have demonstrated great success in scaling up molecular simulations with *ab initio* accuracy, they possess the limitation of lacking interpretable

models for predicted phenomena, leading to unknown accuracy outside the training set. Wen and Tadmor resolve such by proposing the Dropout Uncertainty Neural Network (DUNN) model by eliciting a dropout matrix \mathbf{D} to the original energy formulation by Behler and coworkers (Behler and Parrinello, 2007; Artrith, Morawietz, and Behler, 2011; Artrith and Behler, 2012), writes

$$\begin{aligned} E^{\text{DUNN}} &= \sum_{i=1}^N E_i^{\text{DUNN}}, \\ \longrightarrow E_i^{\text{DUNN}} &= h[h[\mathbf{y}_0(\mathbf{D}_1 \mathbf{W}_1) + \mathbf{b}_1](\mathbf{D}_2 \mathbf{W}_2) + \mathbf{b}_2](\mathbf{D}_3 \mathbf{W}_3) + \mathbf{b}_3 \end{aligned} \quad (12)$$

where \mathbf{D}_i is a square diagonal binary matrix of integers 0 or 1, in which the diagonal follows the Bernoulli distribution (Wen and Tadmor, 2020). With the formulation by Behler and coworkers (Artrith and Behler, 2012), the input layer is transformed through N_{desc} descriptors $g^j(\mathbf{r}_i)$ satisfying the symmetry requirements, with a specified cutoff radius. Note that \mathbf{r}_i can be viewed as describing the local environment within the cutoff.

$$y_0^j = g^j(\mathbf{r}_i), \quad j = 1, 2, \dots, N_{\text{desc}} \quad (13)$$

Now, one can define Equation (12) as the dropout NN with the updated weights $\tilde{\mathbf{W}}_i = \mathbf{D}_i \mathbf{W}_i$, for which the new model is interpreted by Wen and Tadmor as a Bayesian model. In such a model, the prior distribution $p(\omega)$ over parameters $\omega = \{\tilde{\mathbf{W}}_1, \tilde{\mathbf{W}}_2, \tilde{\mathbf{W}}_3, \mathbf{b}_1, \mathbf{b}_2, \mathbf{b}_3\}$ induces the predictive distribution concerning the likelihood $p(\mathbf{Y} | \mathbf{X}, \omega)$ for training data of (\mathbf{X}, \mathbf{Y}) .

$$\begin{aligned} p(\omega | \mathbf{X}, \mathbf{Y}) &\propto p(\mathbf{Y} | \mathbf{X}, \omega)p(\omega), \\ \longrightarrow p(\mathbf{z} | \mathbf{x}^*, \mathbf{X}, \mathbf{Y}) &= \int p(\mathbf{z} | \mathbf{x}^*, \omega)p(\omega | \mathbf{X}, \mathbf{Y})d\omega \end{aligned} \quad (14)$$

where \mathbf{z} is the quantity of interest, and \mathbf{x}^* are the descriptors for a configuration associated with \mathbf{z} . Note that the training process of DUNN differed from MLIP by the fact that the loss function only contains the differences of energy and forces with no stress included (Wen and Tadmor, 2020).

Here, three different types of DUNN (Mingjian Wen, 2019a,b,c) with different dropout rates were adopted to study the equilibration temperature distribution with a smaller portion of the total graphene sheet. The details are further elaborated in Section II C and ESI.

C. Simulation Setup

In the numerical setup, a three-dimensional simulation box with X and Y directional lengths of 50 nm, and Z directional height of 6 nm were set with full periodic boundary conditions on each surface, as shown in Figure 1. To note, the X direction is the armchair direction and Y is the zigzag direction. A thermal gradient was enforced in the Y direction, where the bottom is the heat source and the upper side is the heat sink. A defect is set in the center of the graphene layer, of different lengths to account for the sizing effects of precrack. To perform the crack propagation, a strain rate of 10^9s^{-1} is applied in the X direction, as indicated in the gray shaded arrows in Figure 1.

To investigate the thermo-mechanical coupling behavior, two parameters are tuned in the simulation, precrack length L_C , and thermal gradient differences ΔT . Five different precrack lengths, 1.7217, 3.1974, 4.1812, 5.6569, and 8.1164 nm, both having a width of 0.71 nm, and four different thermal gradient values, 0K, 100K, 200K, and 300K, are probed in the simulations.

The mechanical properties are characterized by stress-strain responses. Using the deformation gradient tensor $\mathbf{F} = \frac{\partial \mathbf{x}}{\partial \bar{\mathbf{x}}}$ described by the reference and current configurations

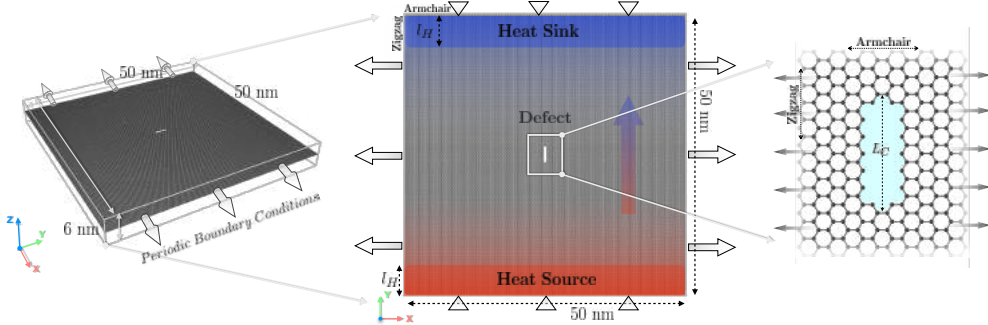


FIG. 1. The schematic view of the numerical setup of the simulation, where a single graphene layer with a preset defect was constrained in the simulation box, with periodic boundary conditions applied on each side. A temperature gradient was set on the two sides of the graphene layer in the Y direction (green arrow). The temperature gradient is created by fixing two constant temperature regions (Heat Sink & Heat Source) of width l_H . Tensile loading of strain rate equals 10^{10} s^{-1} was applied in the X direction (red arrow). The size of the simulation box is $50 \times 50 \times 6 \text{ nm}$ ($X \times Y \times Z$). The defect possesses a morphology of symmetric atomic vacancy, with a specific length and a width of 0.71 nm . L_C stands for the length of the crack (or defect), and the defect is generated by continuously creating a double vacancy and removing their adjacent carbon atoms.

$\mathbf{X} = (X_1, X_2, X_3)$ and $\mathbf{x} = (x_1, x_2, x_3)$, the constitutive model can be written as $\sigma = \Phi(\mathbf{F}(\mathbf{X}, t), \mathbf{X})$. From \mathbf{F} one can derive the displacements, $\mathbf{u} = \mathbf{x} - \mathbf{X}$, from which one can obtain the strain in 3D with indicial notation: $\epsilon_{ij} = \frac{1}{2} \left(\frac{\partial u_i}{\partial X_j} + \frac{\partial u_j}{\partial X_i} \right)$. The strain rate writes

$$\dot{\epsilon}(t) = \frac{d\epsilon}{dt} = \frac{d}{dt} \left(\frac{x_i(t) - X_i}{X_i} \right) \quad (15)$$

Applying the constant strain rate one can record the corresponding stress-strain responses of the graphene layer, where the yield stress writes $\sigma_Y = \max(\sigma(t))$, and the corresponding yield strain takes the form $\epsilon_Y = \Phi^{-1}(\sigma_Y)$.

By performing the simulations using the empirical potentials, three properties are of core interest when studying the mechanism of such non-equilibrium fracture dynamics: the effects of the precrack lengths and thermal gradients, separately, and the thermo-mechanical coupling mechanism on the graphene fracture processes. Here, we apply a high strain rate $\dot{\epsilon} = 10^9 \text{ s}^{-1}$ (10^{-3} ps^{-1}) according to the work of Zhao and Aluru (Zhao and Aluru, 2010), as we hope to (1) benchmark our mechanical responses and compare the results as they also apply such a strain rate to study the fracture of pristine graphene; (2) investigate the coupling mechanism during the fracture process under extreme environments, as the thermal gradient coupled fracture is already a non-equilibrium process. In the study, the main goal is to explore the mechanical responses under extreme environments considering (1) exploring the variabilities of potential models; (2) unveiling the hidden mechanism during the physical process independent of the potentials.

After 10,000 running steps, the calculated temperature distribution along the X position is shown in Figure 2. The four subfigures indicate the temperature distribution along with the X direction position. It can be concluded that the temperature gradient agrees with linear distribution along the area in the mid-region in which the crack propagates. Following the equilibration run, 500,000 steps of tensile loading were carried out while the graphene is soaked in the thermal gradient. The simulation was carried out using the NVE ensemble. (See ESI for the details of implementation in LAMMPS)

For benchmarking the machine learning potentials, two simulation cases were set: (1) when benchmarking the MLIP potential model, we directly replace the empirical potentials with MLIP and carried out the same simulations (See ESI for technical implementation details). (2) In our attempts the DUNN model was not successful in handling deforming boxes

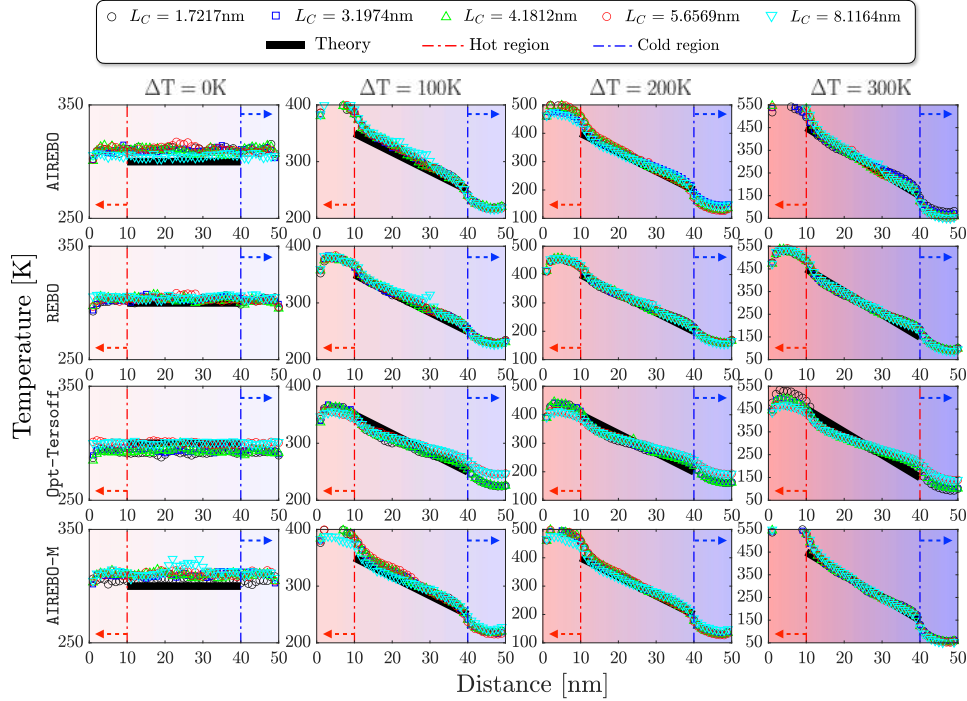


FIG. 2. The temperature distribution along with the single graphene layer after 10,000 steps of equilibration run. The scattered dots in different colors represent different graphene layers with different length of preset crack lengths, as indicated in the legend on the right. The red dashed line and the arrow stands for the boundary of the “heat source” region with higher temperature and the blue dashed line and the arrow stand for the boundary of the “heat sink” region of lower temperature. The theoretical linear temperature fit is marked in the black solid line. Four columns indicate four different temperature gradients and the four rows stand for the temperature distribution under different potential fields.

and high-temperature gradients; and also tends to be more computationally consuming, we hence create a smaller simulation box (length $\sim \frac{1}{5}$ of the original length) and only ran the 10,000 steps of equilibration with zero temperature gradient following the same procedure as before to test the model’s ability to recreate the thermal conditions. Four MLP models, i.e., MLIP (Novikov *et al.*, 2021), DUNN v1 (Mingjian Wen, 2019a), DUNN v2 (Mingjian Wen, 2019b), DUNN v3 (Mingjian Wen, 2019c), are all employed in this case. Note that DUNN v1, v2, and v3, stand for the DUNN with different dropout ratios of 0.1, 0.2, and 0.3, respectively. The details can be found in Ref (Wen and Tadmor, 2020).

III. RESULTS AND DISCUSSION

A. Potentials Effects of Thermomechanical Responses

Figure 3 shows the mechanical responses of graphene sheets with different initial defects under different temperature gradients using different potential fields. Intuitively, one may expect that with a larger initial defect the graphene fractures at lower stress. Observing Figure 3 **A** & **D** one deduces that such trends are not strictly obeyed: the blue and red dots shift back and forth at different temperature gradients. Figure 3 **B** generally obeys the rough trend of crack length correlate with fracture stress and 3 **C** meets the expectation well. One thence deduces that “REBO-related” potentials, i.e., REBO, AIREBO, AIREBO-M, exhibit some unintuitive results that the fracture stresses are not strictly positively

correlated with initial crack length. This point will be further discussed as we characterize the fracture profile in Section III C. The second interesting phenomenon we observe is that the simulations employing the “REBO-based” potentials display strain-hardening effects for graphene with small initial defects, shown in the black dots in Figure 3 **A**, **B** and **D**. We proffer two explanations: (1) The coupling effect of relatively high strain rate and strong attraction between atoms. Equation (5) tells that the attractive forces are switched off for long distances in the REBO energy, whereas under certain strain rate loading as it is still taking effect, the applied stress exhibit the increase as the strain-hardening effect we observed. (2) The transverse bond energy in the X direction further resists the loading. The strain hardening effect is only observed when the initial defect is small in our simulations, where the bond in X direction contributes to resisting the loading. This point will be further elaborated in Section III B. To note, such strain-hardening phenomena are also observed by MD simulations of nanoporous graphene (Cohen-Tanugi and Grossman, 2014; Saumya *et al.*, 2020), graphene nanoribbons (Bu *et al.*, 2009), multilayer graphene (Zhong, Li, and Zhang, 2019), and many.

The temperature is observed to not show an explicit effect on the mechanical responses for different potentials, by comparing Figure 3 **A** to **D**. Suppose the fracture stress is the highest value during loading and the corresponding strain is the fracture strain, under optimized Tersoff potential in Figure 3 **C** higher temperature gradients are reported to reduce the differences between fracture stresses and strains with different initial defects. The AIREBO and REBO potentials in Figure 3 **A** & **B** roughly obey such trends. For AIREBO-M in Figure 3 **D**, higher temperature gradients seem to increase the differences between fracture stresses & strains of different initial defect sizes. In short, no clear mechanism relating to fracture stresses & strains relating to temperature are observed comparing different potentials. The AIREBO and AIREBO-M potentials are reported to exhibit higher fracture stress values and corresponding strains, with the optimized Tersoff and REBO potentials displaying lower fracture stresses & strains.

B. Thermo-Mechanical Coupling Mechanism

Figure 4 shows the relation between the fracture stresses and strains to different initial defect sizes and temperature gradients (See ESI for 3D data visualization contour plot). To verify the result of fracture stresses to defect sizes (in Figure 4 **A**), we apply quantized fracture mechanics (QFM) to fit for fracture intensity K_{IC} for literature comparison. In the work by Pugno and Ruoff (Pugno and Ruoff, 2004), a quantization of Griffith’s criterion is assumed to describe discrete crack propagation, where QFM is the term for such an energy-based method, later showing good compatibility with molecular dynamics (Pugno *et al.*, 2008). Suppose the smallest crack propagation length is L_0 , which for graphene along the zigzag direction should be $L_0 = 0.246\text{nm}$; the initial crack (defect region of graphene) has a length of $L_C = 2\mathfrak{L}$; ρ is the tip radius, which in our case $\rho = 0.265\text{nm}$ (See ESI and (Zhao and Aluru, 2010)). In continuum-based linear elastic fracture mechanics (LEFM), the fracture is defined to occur while the stress intensity equals its critical value, $K_I^{\text{LEFM}} = K_{IC}$ (Irwin, 1957). In QFM, the crack propagates when (Pugno and Ruoff, 2004)

$$K_I^{\text{QFM}} = \sqrt{\frac{1}{L_0} \int_{\mathfrak{L}}^{\mathfrak{L}+L_0} [K_I^{\text{LEFM}}(\mathfrak{L})]^2 d\mathfrak{L}} = K_{IC} \quad (16)$$

Substituting this K_{IC} , the fracture stress in QFM writes $\sigma_F(\mathfrak{L}) = \frac{K_{IC}}{\sqrt{\pi(\mathfrak{L}+L_0/2)}}$, By extending this fracture stress from sharp to blunt cracks (Drory *et al.*, 1995; Creager and Paris, 1967), Ref (Pugno and Ruoff, 2004) finds an asymptotic correction for small tip radii and proposed the form:

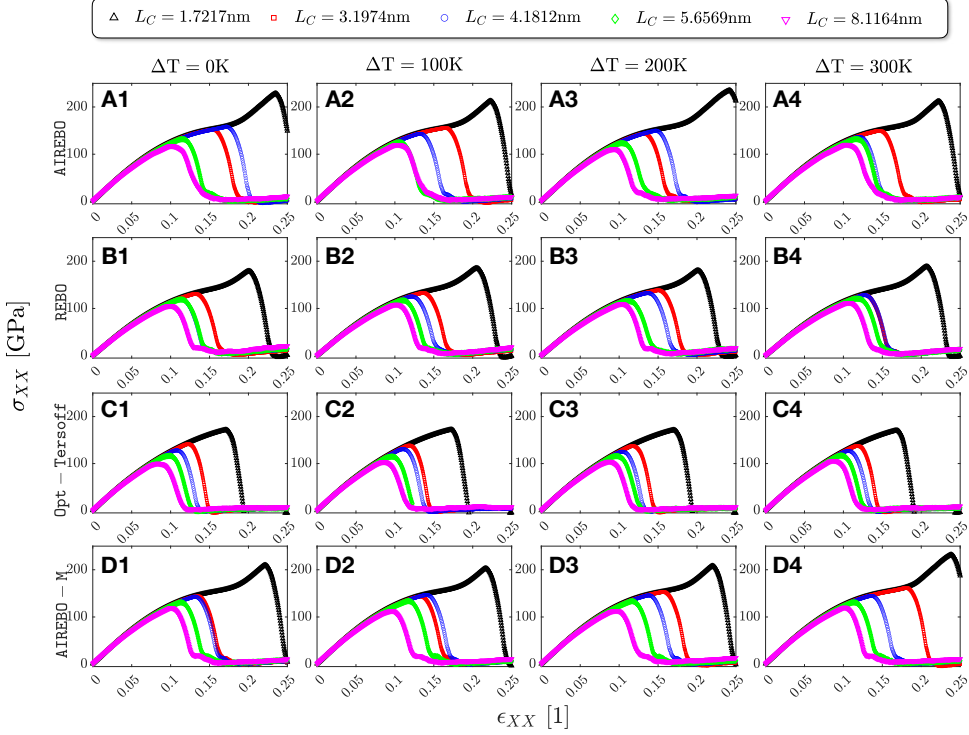


FIG. 3. The stress-strain responses of the graphene sheet during non-equilibrium tensile tests of high strain rate under heat gradients. Subfigures **A**, **B**, **C**, **D** stand for the simulations using AIREBO, REBO, optimized Tersoff, and AIREBO-M potential fields, respectively, as indicated in the labels. The corresponding suffices **1**, **2**, **3**, **4** stand for different temperature gradients as indicated in the titles. Lines of different colors stand for graphene sheets of different initial defects as shown in the legend.

$$\sigma_F(\mathfrak{L}, \rho) = K_{IC} \sqrt{\frac{1 + \frac{\rho}{2L_0}}{\pi(\mathfrak{L} + \frac{L_0}{2})}} \quad (17)$$

We use Equation (17) as the form for calculating the critical stress intensity. Our K_{IC} for the four potentials are approximately 9.49, 8.85, 8.85, 9.49 MPa \sqrt{m} , similar with the value of 9.2 ± 0.8 MPa \sqrt{m} of fracture direction $\sim 73^\circ$ of monolayer in Ref (Zhao *et al.*, 2022) and $10.7 \sim 14$ MPa \sqrt{m} of CVD-grown graphene (Hwangbo *et al.*, 2014). Yet, the results seem to be larger than the experimental value of 4.0 ± 0.6 MPa \sqrt{m} by Zhang *et al.* (Zhang *et al.*, 2014) and smaller than 12 ± 3.9 MPa \sqrt{m} of multiplayer graphene (Wei *et al.*, 2015). Taking the value in (Zhao *et al.*, 2022) as benchmarks, our calculated values have relative errors of 3.15%, 3.80%, 3.80%, 3.15%, respectively, indicating our calculations are generally accurate. Based on our fitted K_{IC} , the curve representing QFM matching our simulation data are shown in Figure 4 **A** in the right top corner as the light blue dotted lines. The theory matches our data well.

We also provide a new perspective regarding the phenomenon observed in Figure 4 **A**: for larger initial cracks, the fracture stresses seem to decrease in a milder trend. To illustrate, the gray dashed arrows depict the mild decreasing trend as the crack length increases, whilst the pink dashed arrows specify the nonlinear “suddenly” increasing trend of the shorter crack. We proffer that for shorter cracks, the horizontal (X direction) component of the crack edge bond force shares the loading along the crack tip and further increases the fracture stress, accounting for the nonlinear increase of the fracture stress. For longer

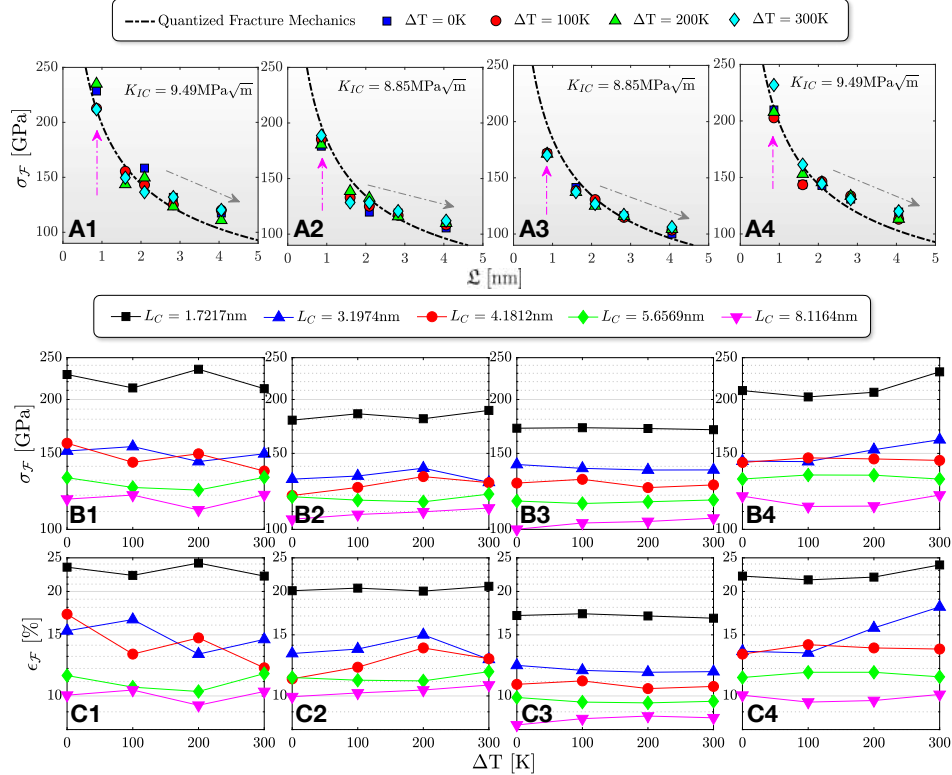


FIG. 4. The diagrams of the fracture stresses and strains (σ_F & ϵ_F) of the graphene layer regarding different initial defects lengths and temperature differences. **A.** The fracture stresses in relation to initial defect length, with the fitted curve by quantized fracture mechanics marked in black dashed line. The corresponding values under different temperature gradients are marked in different shaped dots of different colors. The fitted fracture intensities K_{IC} are marked on the right-top corners of each subfigure. **B.** The fracture stress relations to temperature gradients. **C.** The fracture strains relations to temperature gradients. Note that for **B** and **C** each colored dotted line indicate a specific initial crack length, marked in the legend on top.

initial cracks, more forces are concentrated on the crack tip and the bond force share less of the applied loading, which explains the milder fracture stress decreasing trend as initial cracks are longer. To illustrate, Figure 5 shows the fracture process with initial crack $L_C = 1.7217\text{nm}$ corresponding to the stress-strain responses. For both the four potentials, comparing the morphology of the cracks before and after the fractured moment (red star) it can be observed that the crack width is pulled aside for the bond connecting the crack tip to share the load. What's more, comparing Figure 5 **A** & **D** with **B** & **C** we observe that for AIREBO and AIREBO-M the defect is loaded to a larger extent compared with REBO and optimized Tersoff: (1) the longest pulled width is longer by observing the defect morphology preceding to the fractured moment (2) the fracture strain corresponds to the red star is higher.

Equations (2) and (4) tell us that the REBO and Tersoff models follow similar formulations: the atomic interactions can be considered as linearly combinations of repulsion and attractions. The attractive terms in REBO (Equation (5)) are switched off for long-distanced interactions and the weight function f_{ij}^C ensures atomic interactions are canceled outside the cutoff range. Equations (6) and (9) contend that the AIREBO and AIREBO-M potentials contain extra torsion energy, Leonard-Jones and/or Morse energies compared with the pure REBO model. We hence propose that these extra energies account for the better loading duration for AIREBO & AIREBO-M compared with the optimized Tersoff and REBO models in Figure 5. Figure 5 **B** & **C** indicates that no clear relation can be

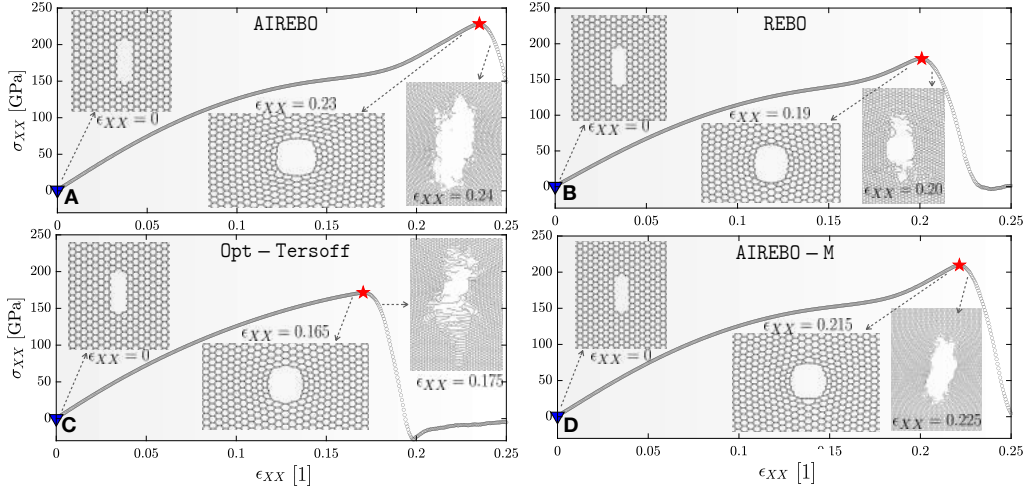


FIG. 5. The stress-strain responses of the graphene sheet using the four different potential fields of a small initial defect ($L_C = 1.7217\text{nm}$). The four subfigures **A**, **B**, **C**, **D** illustrated the deformation and fracture profile along the defected area marked with the corresponding strain values. The red star stands for the fractured moment. The blue triangular dot is the initial morphology of the defect.

concluded between the temperature gradients and fracture stresses & strains, agrees with the trend we concluded in Figure 3.

C. Fracture Characterizations

In the experiments, all the initial crack propagation profiles are observed for different initial defects under different temperature gradients under different potential fields (Details see ESI). Observations indicate that the initial crack propagation directions are not guided by the temperature gradients. An interesting phenomenon of kinetic energy transportation along the crack tip is observed and characterized in Figure 6, depicted by 6 representative cases, illustrated from subfigures **A** to **F**. Theoretically, the kinetic energy in the fracture can be perceived as the difference between the released strain energy and surface energy that drives the crack propagation, whilst the propagating stops when the accumulated kinetic energy approaches zero (Guo *et al.*, 2015). Intuitively, one expects the crack to start propagating when the kinetic energy accumulates on one side to drive the crack propagation. However, an unexpected phenomenon of the kinetic energy transport from the initial accumulation side to another side that further drives the crack propagation is observed among the REBO, AIREBO, and AIREBO-M potentials. Figure 6 **A**, **B**, **C**, & **E** illustrate such processes for AIREBO, REBO, AIREBO-M, under different temperature gradients (See caption). Regarding Equations (4), (6), & (9), we propose that this anomalous fracture behavior observed among the “REBO-based” potentials may attribute to the strong short-range attraction: the short-ranged strong attraction force resist the crack propagating on the kinetic energy accumulation side initially, then the released strain energy is transported to the other side of crack tips. The applied load elongates the loading directions, canceling some short-ranged attractions and further inducing the crack propagation on this side. The observation results of this anomalous fracture phenomena indicate that for higher temperature gradients of longer initial cracks, the phenomena are more frequently observed, and the phenomena are more frequently observed for AIREBO & AIREBO-M potentials (Refer to Table S2 in ESI).

The visualizations indicate that the crack propagation does not strictly follow the brittle fracture scenario: the crack does not propagate in a “sharped cut” shape benchmarking Ref

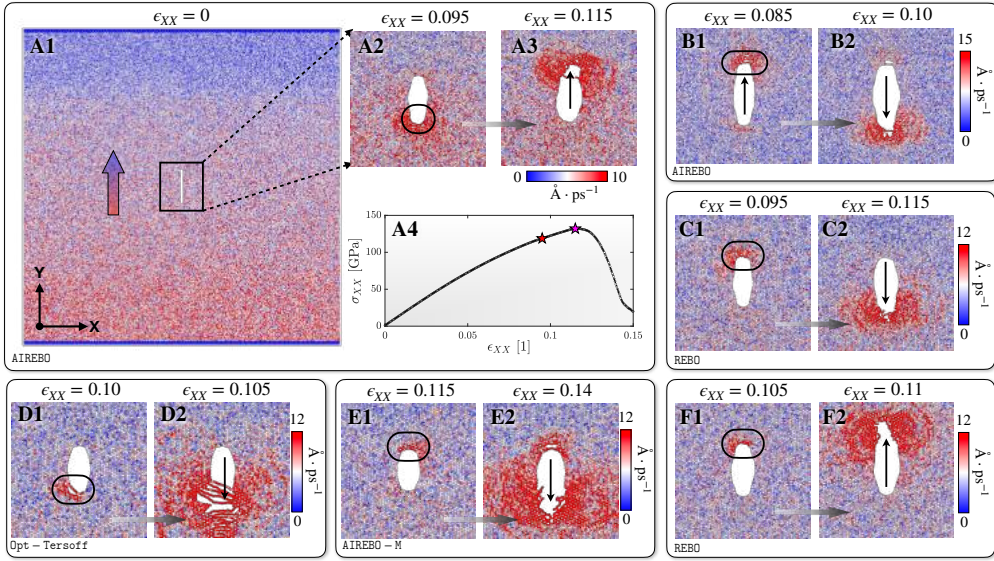


FIG. 6. Graphical illustration of the observed “energy transportation” phenomena during the fracture process. The subfigures **A** to **F** stand for the 6 representative simulation cases to depict the fracture processes. **A1** to **A3** illustrates a typical observed energy transportation process of higher kinetic energy first clustered as one side of crack tip the, and **A4** is a stress-strain response corresponding the process, for which the red and pink stars corresponds to **A2** and **A3**, respectively. The simulation is implemented with the AIREBO potential under a 300K temperature gradient. **B**. The anomalous fracture observed under a 0K temperature gradient with the AIREBO potential. **C**. The anomalous fracture observed with the REBO potential. **D**. A normal fracture observed with the optimized Tersoff potential. **E**. The anomalous fracture observed with the AIREBO-M potential. **F**. A normal fracture observed with the REBO potential. Note that the color bar indicates the atomic velocities, in $\text{\AA}\cdot\text{ps}^{-1}$.

(Zhang *et al.*, 2014). Note that Zhang et al. (Zhang *et al.*, 2014) adopt an initial defect of 10nm, which is larger than our largest initial defect (8.1164nm). It is indicated by Hu et al. (Hu *et al.*, 2015) that porous graphene exhibits crack tip blunting behavior. Hence, we propose that the short crack in our simulations can be viewed as an analog of the circular pore, indicating the blunting behavior may attribute to the higher width-to-length aspect ratio. The initial fracture of longer cracks is observed to be closer to pure brittle fractures (See ESI). However, in either way, the optimized Tersoff model does not seem to be an ideal model to adopt for modeling the mechanical behaviors of graphene, as they exhibit “crazing-like” fractures (See ESI), which should not be expected for graphene.

D. Benchmarking Machine Learning Potentials

Given our designed numerical experiments in Section II C, the results for benchmarking different MLPs are shown in Figure 7. There are no clear relations that can be concluded between the mechanical responses to temperature gradients using the MLIP potential in Figure 7 **A**, which agrees with the observation in Figure 3. Figure 7 **B** suggests that the MLIP potential exhibit evidently smaller fracture stress, comparing with four empirical potentials, under four different temperature gradients. If we compute the average value of the four empirical models under the four temperature gradients for benchmarking the MLIP fracture stress, we have $\sigma_f^{\text{MLIP}} \approx 0.39\sigma_f^{\text{REBO}}$, $\sigma_f^{\text{MLIP}} \approx 0.32\sigma_f^{\text{AIREBO}}$, $\sigma_f^{\text{MLIP}} \approx 0.33\sigma_f^{\text{AIREBO-M}}$. Figure 7 **C** shows the benchmark tests of four different machine learning potentials for running the basic equilibration test in a small box, where we employ the optimized Tersoff as a benchmark since it is reported to have a more accurate thermal properties descriptions

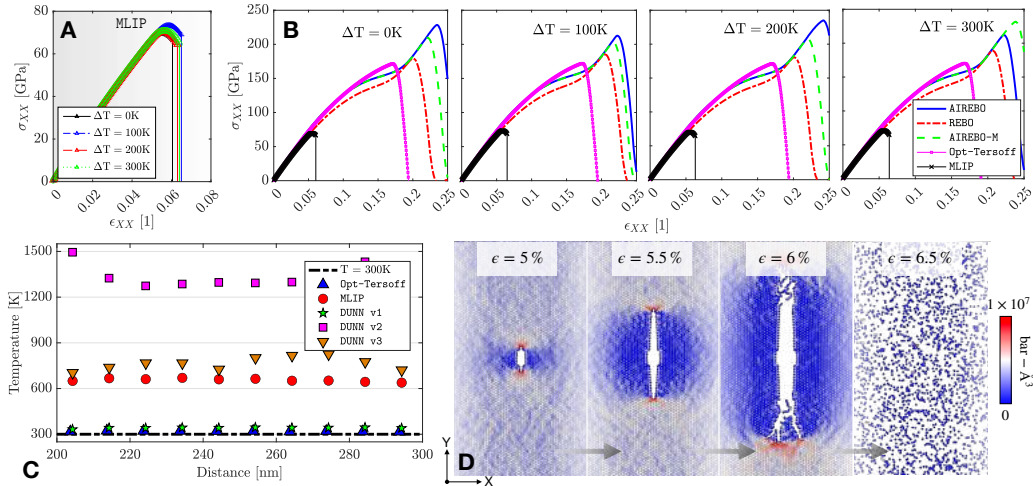


FIG. 7. The simulation results for benchmarking the machine learning methods. **A.** The stress-strain responses of the graphene fracture with small defect ($L_C = 1.7217\text{nm}$) using the MLIP potential, in which different temperature gradient environments are marked in different colors shown in the legend. **B.** The stress-strain responses comparing the four empirical potentials with MLIP on fracturing the graphene sheet with the small defect, in which different colored lines stand for different potentials indicated in the legend. **C.** The temperature distribution after 10,000 steps of equilibration run with preset 300K constant temperature, where different colored and shaped dots stand for different ML potentials. The optimized Tersoff potential is employed to benchmark the results in blue triangular dots and theoretical values are indicated as the dashed line at the bottom. **D.** Graphical representation of a typical fracture process based on MLIP potential. The selected process is when $\Delta T = 300\text{K}$, where the corresponding strains are marked on top. Virial atomic stresses are expressed in units of bar- \AA^3 (See color bar).

than AIREBO and AIREBO-M (Si *et al.*, 2017). Results in Figure 7 **C** suggest that DUNN with a dropout rate of 0.2 (DUNN v2) has the most accurate energy configuration indicated in the green stars. DUNN with the dropout rate of 0.1 has similar accuracy to MLIP, and DUNN v3 does not exhibit a decent energy configuration. Investigation of the influence of the dropout ratio on the final configuration and various properties of graphene might be an interesting future direction.

Figure 7 **D** shows the graphical illustration of the fracture profile by employing the MLIP potential. Note that the MLIP fractures under different temperature gradients are observed to exhibit similar characteristics where we pick $\Delta T = 300\text{K}$ only to represent the process. It is observed that the fracture happened at a strain value around $\epsilon = 5\%$, which is $\frac{1}{3}$ of the traditional potentials with a similar initial defect size (Refer to ESI for the initial fracture profile). The fracture process employ MLIP is observed to be a pure brittle fracture, matches with the experimental results (Zhang *et al.*, 2019) and molecular dynamics simulations (Zhang *et al.*, 2014). Immediately after the fracture happens, the graphene sheet “exploded” into scatter carbon atoms indicated when $\epsilon = 6.5\%$ in Figure 7 **D**. This result indicates the MLIP potential lacks post-fracture descriptions, which can possibly be attributed to the lack of relevant training data while constructing the model.

IV. CONCLUSION AND OUTLOOK

We employ non-equilibrium molecular dynamics to study the fracture behavior of graphene sheets under thermal gradients by employing different potential models, using the LAMMPS software (Plimpton, 1995). A simulation box with periodic boundary conditions containing a single graphene layer with different sizes of initial defects under

different thermal gradients is set up to study. We are essentially interested in answering three main questions: (1) What is the effect of the potential field on simulating the thermo-mechanical behavior of graphene? (2) What are the underlying mechanisms of fracture under extreme environments, i.e., high strain rate coupling thermal gradient, dependent and independent of potential models? (3) What are initial fracture characteristics and whether they are controlled by the thermal gradients and potential fields? Other than that, we are also curious whether our simulations at the molecular scale in non-equilibrium match the theory of fracture mechanics. What's more, we also apply the state-of-the-art *ab initio* based machine learning potential fields to benchmark our simulations with empirical potentials and discuss the characteristics of the machine learning potentials. The further investigations provide a unique multiscale perspective from the first principle, to molecular, to the sub-continuum scale.

On the effects of the potential fields, we found (1) For AIREBO & AIREBO-M, the fracture stresses are not positively correlated with the initial defect size; (2) The strain-hardening effects are observed for “REBO-based” potentials; (3) The temperature gradients do not seem to have a direct effect on the mechanical responses considering both the potential models; (4) The AIREBO and AIREBO-M potentials exhibit higher fracture stresses compared with optimized Tersoff and REBO potentials. For (2), we think that both coupling effects of high strain rate with atomic attractions and transverse bond force attribute to the strain-hardening. On the thermo-mechanical mechanism of graphene fracture, we verify our molecular dynamics simulation with quantized fracture mechanics. We provide a novel perspective of a nonlinear increase of fracture stress regarding smaller initial crack length: the transverse bond force shares the loading. What's more, the AIREBO and AIREBO-M potentials are estimated to exhibit stronger attraction, leading to higher bond force based on the observations of wider crack morphology preceding the fracture. The fracture stresses and strains are reported to not be related to temperature gradients. Also, the initial fracture directions and propagation are observed to be not related to the temperature gradients. Interestingly, an anomalous fracture form of kinetic energy transportation along the crack tips is observed and explanations based on fracture mechanics are proposed. Based on the observation, the optimized Tersoff model does not seem to be an accurate model to characterize the fracture behaviors. We also propose that the blunting effects of the short crack may attribute to the strain-hardening effects observed previously. The MLIP potential displays smaller fracture stress (a little more than $\frac{1}{3}$ of the empirical potentials) on the simulations with the small initial crack. The fracture processes employing MLIP are observed to be pure brittle fractures, yet the atoms “exploded” right after the fracture. Benchmarking the four machine learning potentials indicate dropout uncertainty neural network with a dropout rate of 0.2 has a better energy configuration accuracy than the rest, taking optimized Tersoff potential as a benchmark model.

In brief, our work investigates the thermo-mechanical coupling mechanism of graphene fracture under thermal gradients from the multiscale employing tools of molecular dynamics, fracture mechanics, and machine learning models. Our study is expected to fill the vacancy of (1) characterizing the graphene’s extreme mechanical behavior under heat gradients in non-equilibrium. (2) benchmark different machine learning potentials for molecular simulations. The work can potentially inspire further studies and guide general industrial applications, such as fatigue and damage in graphene-based batteries, biosensors, etc.

DATA AVAILABILITY

The data and code used in this paper are available upon reasonable request to the authors.

ACKNOWLEDGEMENT

The authors acknowledge support from the US National Science Foundation (Grant No. 2038057), Cornell University's Cornell-China Center, and faculty startup grant. The authors also acknowledge computational resources provided by the XSEDE program under Grant TG-MAT200004 and TG-BIO210063, and computational resources provided by Graphite and G2 cluster from Cornell University.

REFERENCES

- Akinwande, D., Brennan, C. J., Bunch, J. S., Egberts, P., Felts, J. R., Gao, H., Huang, R., Kim, J.-S., Li, T., Li, Y., Liechti, K. M., Lu, N., Park, H. S., Reed, E. J., Wang, P., Yakobson, B. I., Zhang, T., Zhang, Y.-W., Zhou, Y., and Zhu, Y., "A review on mechanics and mechanical properties of 2d materials—graphene and beyond," *Extreme Mechanics Letters* **13**, 42–77 (2017).
- Ando, T., "The electronic properties of graphene and carbon nanotubes," *NPG Asia Materials* **1**, 17–21 (2009).
- Araujo, P. T., Terrones, M., and Dresselhaus, M. S., "Defects and impurities in graphene-like materials," *Materials Today* **15**, 98–109 (2012).
- Artrith, N. and Behler, J., "High-dimensional neural network potentials for metal surfaces: A prototype study for copper," *Physical Review B* **85** (2012), 10.1103/physrevb.85.045439.
- Artrith, N., Morawietz, T., and Behler, J., "High-dimensional neural-network potentials for multicomponent systems: Applications to zinc oxide," *Physical Review B* **83** (2011), 10.1103/physrevb.83.153101.
- Bagri, A., Kim, S.-P., Ruoff, R. S., and Shenoy, V. B., "Thermal transport across twin grain boundaries in polycrystalline graphene from nonequilibrium molecular dynamics simulations," *Nano Letters* **11**, 3917–3921 (2011).
- Balandin, A. A., "Thermal properties of graphene and nanostructured carbon materials," *Nature Materials* **10**, 569–581 (2011).
- Balandin, A. A., Ghosh, S., Bao, W., Calizo, I., Teweldebrhan, D., Miao, F., and Lau, C. N., "Superior thermal conductivity of single-layer graphene," *Nano Letters* **8**, 902–907 (2008).
- Behler, J. and Parrinello, M., "Generalized neural-network representation of high-dimensional potential-energy surfaces," *Physical Review Letters* **98** (2007), 10.1103/physrevlett.98.146401.
- Boretti, A., Al-Zubaidy, S., Vaclavikova, M., Al-Abri, M., Castelletto, S., and Mikhalovsky, S., "Outlook for graphene-based desalination membranes," *npj Clean Water* **1** (2018).
- Brenner, D. W., "Empirical potential for hydrocarbons for use in simulating the chemical vapor deposition of diamond films," *Physical Review B* **42**, 9458–9471 (1990).
- Brenner, D. W., "Erratum: Empirical potential for hydrocarbons for use in simulating the chemical vapor deposition of diamond films," *Physical Review B* **46**, 1948–1948 (1992).
- Brenner, D. W., Shenderova, O. A., Harrison, J. A., Stuart, S. J., Ni, B., and Sinnott, S. B., "A second-generation reactive empirical bond order (REBO) potential energy expression for hydrocarbons," *Journal of Physics: Condensed Matter* **14**, 783–802 (2002).
- Bu, H., Chen, Y., Zou, M., Yi, H., Bi, K., and Ni, Z., "Atomistic simulations of mechanical properties of graphene nanoribbons," *Physics Letters A* **373**, 3359–3362 (2009).
- Bunch, J. S., *Mechanical and electrical properties of graphene sheets* (Citeseer, 2008).
- Chen, H., Xu, H., Wang, S., Huang, T., Xi, J., Cai, S., Guo, F., Xu, Z., Gao, W., and Gao, C., "Ultrafast all-climate aluminum-graphene battery with quarter-million cycle life," *Science Advances* **3** (2017).
- Cohen-Tanugi, D. and Grossman, J. C., "Mechanical strength of nanoporous graphene as a desalination membrane," *Nano Letters* **14**, 6171–6178 (2014).
- Creager, M. and Paris, P. C., "Elastic field equations for blunt cracks with reference to stress corrosion cracking," *International Journal of Fracture Mechanics* **3**, 247–252 (1967).
- David, C., "The morse potential," (2003), physical Chemistry 351 at the University of Connecticut.
- Drory, M. D., Dauskardt, R. H., Kant, A., and Ritchie, R. O., "Fracture of synthetic diamond," *Journal of Applied Physics* **78**, 3083–3088 (1995).
- Felix, L. C., Tromer, R. M., Autreto, P. A. S., Junior, L. A. R., and Galvao, D. S., "On the mechanical properties and thermal stability of a recently synthesized monolayer amorphous carbon," *The Journal of Physical Chemistry C* **124**, 14855–14860 (2020).
- Ferrante, J., Smith, J. R., and Rose, J. H., "Diatomeric molecules and metallic adhesion, cohesion, and chemisorption: A single binding-energy relation," *Phys. Rev. Lett.* **50**, 1385–1386 (1983).
- Gao, X., Ramezanghorbani, F., Isayev, O., Smith, J. S., and Roitberg, A. E., "TorchANI: A free and open source PyTorch-based deep learning implementation of the ANI neural network potentials," *Journal of Chemical Information and Modeling* **60**, 3408–3415 (2020).
- Grantab, R., Shenoy, V. B., and Ruoff, R. S., "Anomalous strength characteristics of tilt grain boundaries in graphene," *Science* **330**, 946–948 (2010).
- Gu, X., Wei, Y., Yin, X., Li, B., and Yang, R., "Colloquium: Phononic thermal properties of two-dimensional materials," *Rev. Mod. Phys.* **90**, 041002 (2018).

- Guo, L., Kitamura, T., Yan, Y., Sumigawa, T., and Huang, K., "Fracture mechanics investigation on crack propagation in the nano-multilayered materials," *International Journal of Solids and Structures* **64-65**, 208–220 (2015).
- Hashimoto, A., Suenaga, K., Gloter, A., Urita, K., and Iijima, S., "Direct evidence for atomic defects in graphene layers," *Nature* **430**, 870–873 (2004).
- Homaeigohar, S. and Elbahri, M., "Graphene membranes for water desalination," *NPG Asia Materials* **9**, e427–e427 (2017).
- Hu, J., Ruan, X., and Chen, Y. P., "Thermal conductivity and thermal rectification in graphene nanoribbons: A molecular dynamics study," *Nano Letters* **9**, 2730–2735 (2009).
- Hu, J., Zhou, J., Zhang, A., Yi, L., and Wang, J., "Temperature dependent mechanical properties of graphene based carbon honeycombs under tension and compression," *Physics Letters A* **391**, 127130 (2021).
- Hu, L., Wyant, S., Muniz, A. R., Ramasubramaniam, A., and Maroudas, D., "Mechanical behavior and fracture of graphene nanomeshes," *Journal of Applied Physics* **117**, 024302 (2015).
- Hwangbo, Y., Lee, C.-K., Kim, S.-M., Kim, J.-H., Kim, K.-S., Jang, B., Lee, H.-J., Lee, S.-K., Kim, S.-S., Ahn, J.-H., and Lee, S.-M., "Fracture characteristics of monolayer CVD-graphene," *Scientific Reports* **4** (2014), 10.1038/srep04439.
- Irwin, G. R., "Analysis of stresses and strains near the end of a crack traversing a plate," *Journal of Applied Mechanics* **24**, 361–364 (1957).
- Jangid, P. and Kottanthalayil, A., "Reconstruction of fractured graphene by thermal treatment in methane gas," *Materials Science and Engineering: B* **260**, 114625 (2020).
- Jung, G. S., Myung, H. J., and Irle, S., "Artificial neural network potentials for mechanics and fracture dynamics of materials," (2022).
- Jung, G. S., Yeo, J., Tian, Z., Qin, Z., and Buehler, M. J., "Unusually low and density-insensitive thermal conductivity of three-dimensional gyroid graphene," *Nanoscale* **9**, 13477–13484 (2017).
- Kasirga, T. S., "Thermal conductivity measurements in 2d materials," in *Thermal Conductivity Measurements in Atomically Thin Materials and Devices* (Springer Singapore, 2020) pp. 11–27.
- Lee, C., Wei, X., Kysar, J. W., and Hone, J., "Measurement of the elastic properties and intrinsic strength of monolayer graphene," *Science* **321**, 385–388 (2008).
- Li, M., Deng, T., Zheng, B., Zhang, Y., Liao, Y., and Zhou, H., "Effect of defects on the mechanical and thermal properties of graphene," *Nanomaterials* **9** (2019).
- Lindsay, L. and Broido, D. A., "Optimized tersoff and brener empirical potential parameters for lattice dynamics and phonon thermal transport in carbon nanotubes and graphene," *Physical Review B* **81** (2010).
- Liu, K. and Wu, J., "Mechanical properties of two-dimensional materials and heterostructures," *Journal of Materials Research* **31**, 832–844 (2016).
- Liu, P., Li, X., Min, P., Chang, X., Shu, C., Ding, Y., and Yu, Z.-Z., "3d lamellar-structured graphene aerogels for thermal interface composites with high through-plane thermal conductivity and fracture toughness," *Nano-Micro Letters* **13** (2020).
- Mahdizadeh, S. J. and Akhlaghi, G., "Optimized tersoff empirical potential for germanene," *Journal of Molecular Graphics and Modelling* **72**, 1–5 (2017).
- Mingjian Wen, "Dropout uncertainty neural network (dunn) potential for condensed-matter carbon systems developed by wen and tadmor (2019) v000," (2019a).
- Mingjian Wen, "Dropout uncertainty neural network (dunn) potential for condensed-matter carbon systems developed by wen and tadmor (2019) v000," (2019b).
- Mingjian Wen, "Dropout uncertainty neural network (dunn) potential for condensed-matter carbon systems developed by wen and tadmor (2019) v000," (2019c).
- Mortazavi, B., Rajabpour, A., Zhuang, X., Rabczuk, T., and Shapeev, A. V., "Exploring thermal expansion of carbon-based nanosheets by machine-learning interatomic potentials," *Carbon* **186**, 501–508 (2022).
- Mortazavi, B., Silani, M., Podryabinkin, E. V., Rabczuk, T., Zhuang, X., and Shapeev, A. V., "First-principles multiscale modeling of mechanical properties in graphene/borophene heterostructures empowered by machine-learning interatomic potentials," *Advanced Materials* **33**, 2102807 (2021).
- Ng, T., Yeo, J., and Liu, Z., "A molecular dynamics study of the thermal conductivity of graphene nanoribbons containing dispersed stone–thrower–wales defects," *Carbon* **50**, 4887–4893 (2012).
- Novikov, I., Grabowski, B., Körmann, F., and Shapeev, A., "Magnetic moment tensor potentials for collinear spin-polarized materials reproduce different magnetic states of bcc fe," *npj Computational Materials* **8** (2022), 10.1038/s41524-022-00696-9.
- Novikov, I. S., Gubaev, K., Podryabinkin, E. V., and Shapeev, A. V., "The MLIP package: moment tensor potentials with MPI and active learning," *Machine Learning: Science and Technology* **2**, 025002 (2021).
- Novoselov, K. S., Geim, A. K., Morozov, S. V., Jiang, D., Zhang, Y., Dubonos, S. V., Grigorieva, I. V., and Firsov, A. A., "Electric field effect in atomically thin carbon films," *Science* **306**, 666–669 (2004).
- Obeng, Y. and Srinivasan, P., "Graphene: Is it the future for semiconductors? an overview of the material, devices, and applications," *Interface magazine* **20**, 47–52 (2011).
- O'Connor, T. C., Andzelm, J., and Robbins, M. O., "AIREBO-m: A reactive model for hydrocarbons at extreme pressures," *The Journal of Chemical Physics* **142**, 024903 (2015).
- Papageorgiou, D. G., Kinloch, I. A., and Young, R. J., "Mechanical properties of graphene and graphene-based nanocomposites," *Progress in Materials Science* **90**, 75–127 (2017).

- Plimpton, S., "Fast parallel algorithms for short-range molecular dynamics," *Journal of computational physics* **117**, 1–19 (1995).
- Pugno, N., Carpinteri, A., Ippolito, M., Mattoni, A., and Colombo, L., "Atomistic fracture: QFM vs. MD," *Engineering Fracture Mechanics* **75**, 1794–1803 (2008).
- Pugno, N. M. and Ruoff, R. S., "Quantized fracture mechanics," *Philosophical Magazine* **84**, 2829–2845 (2004).
- Rose, J. H., Smith, J. R., and Ferrante, J., "Universal features of bonding in metals," *Phys. Rev. B* **28**, 1835–1845 (1983).
- Saumya, K., Gupta, K. K., Roy, A., and Dey, S., "Effect of spatial distribution of nanopores on mechanical properties of mono layer graphene," *IOP Conference Series: Materials Science and Engineering* **872**, 012187 (2020).
- Shareena, T. P. D., McShan, D., Dasmahapatra, A. K., and Tchounwou, P. B., "A review on graphene-based nanomaterials in biomedical applications and risks in environment and health," *Nano-Micro Letters* **10** (2018).
- Si, C., Wang, X.-D., Fan, Z., Feng, Z.-H., and Cao, B.-Y., "Impacts of potential models on calculating the thermal conductivity of graphene using non-equilibrium molecular dynamics simulations," *International Journal of Heat and Mass Transfer* **107**, 450–460 (2017).
- Song, H., Liu, J., Liu, B., Wu, J., Cheng, H.-M., and Kang, F., "Two-dimensional materials for thermal management applications," *Joule* **2**, 442–463 (2018).
- Stuart, S. J., Tutein, A. B., and Harrison, J. A., "A reactive potential for hydrocarbons with intermolecular interactions," *The Journal of Chemical Physics* **112**, 6472–6486 (2000).
- Tersoff, J., "New empirical model for the structural properties of silicon," *Phys. Rev. Lett.* **56**, 632–635 (1986).
- Tersoff, J., "New empirical approach for the structure and energy of covalent systems," *Physical Review B* **37**, 6991–7000 (1988).
- Wan, S., Chen, Y., Fang, S., Wang, S., Xu, Z., Jiang, L., Baughman, R. H., and Cheng, Q., "High-strength scalable graphene sheets by freezing stretch-induced alignment," *Nature Materials* **20**, 624–631 (2021).
- Wang, C., Li, D., Too, C. O., and Wallace, G. G., "Electrochemical properties of graphene paper electrodes used in lithium batteries," *Chemistry of Materials* **21**, 2604–2606 (2009).
- Wang, H., Zhang, L., Han, J., and E, W., "DeePMD-kit: A deep learning package for many-body potential energy representation and molecular dynamics," *Computer Physics Communications* **228**, 178–184 (2018).
- Wei, X. and Kysar, J. W., "Experimental validation of multiscale modeling of indentation of suspended circular graphene membranes," *International Journal of Solids and Structures* **49**, 3201–3209 (2012).
- Wei, X., Xiao, S., Li, F., Tang, D.-M., Chen, Q., Bando, Y., and Golberg, D., "Comparative fracture toughness of multilayer graphenes and boronitrenes," *Nano Letters* **15**, 689–694 (2015).
- Wei, Y., Wu, J., Yin, H., Shi, X., Yang, R., and Dresselhaus, M., "The nature of strength enhancement and weakening by pentagon–heptagon defects in graphene," *Nature Materials* **11**, 759–763 (2012).
- Wei, Y. and Yang, R., "Nanomechanics of graphene," *National Science Review* **6**, 324–348 (2018).
- Wen, M. and Tadmor, E. B., "Hybrid neural network potential for multilayer graphene," *Physical Review B* **100** (2019), 10.1103/physrevb.100.195419.
- Wen, M. and Tadmor, E. B., "Uncertainty quantification in molecular simulations with dropout neural network potentials," *npj Computational Materials* **6** (2020), 10.1038/s41524-020-00390-8.
- Xie, C., Wang, Y., Zhang, Z.-X., Wang, D., and Luo, L.-B., "Graphene/semiconductor hybrid heterostructures for optoelectronic device applications," *Nano Today* **19**, 41–83 (2018).
- Xu, L., Wei, N., Zheng, Y., Fan, Z., Wang, H.-Q., and Zheng, J.-C., "Graphene-nanotube 3d networks: intriguing thermal and mechanical properties," *J. Mater. Chem.* **22**, 1435–1444 (2012).
- Xu, Z. and Buehler, M. J., "Strain controlled thermomutability of single-walled carbon nanotubes," *Nanotechnology* **20**, 185701 (2009).
- Yang, Y., Asiri, A. M., Tang, Z., Du, D., and Lin, Y., "Graphene based materials for biomedical applications," *Materials Today* **16**, 365–373 (2013).
- Yanovsky, Y., Nikitina, E., Karnet, Y., and Nikitin, S., "Quantum mechanics study of the mechanism of deformation and fracture of graphene," *Physical Mesomechanics* **12**, 254–262 (2009).
- Yoo, B., Xu, Z., and Ding, F., "How single-walled carbon nanotubes are transformed into multiwalled carbon nanotubes during heat treatment," *ACS Omega* **6**, 4074–4079 (2021).
- Yuan, H. and Kalkhof, D., "Effects of temperature gradients on crack characterisation under thermal-mechanical loading conditions," *International Journal of Fracture* **100**, 355–377 (2000).
- Zhang, J., Zhao, J., and Lu, J., "Intrinsic strength and failure behaviors of graphene grain boundaries," *ACS Nano* **6**, 2704–2711 (2012).
- Zhang, L., Han, J., Wang, H., Car, R., and E, W., "Deep potential molecular dynamics: A scalable model with the accuracy of quantum mechanics," *Physical Review Letters* **120** (2018), 10.1103/physrevlett.120.143001.
- Zhang, P., Ma, L., Fan, F., Zeng, Z., Peng, C., Loya, P. E., Liu, Z., Gong, Y., Zhang, J., Zhang, X., Ajayan, P. M., Zhu, T., and Lou, J., "Fracture toughness of graphene," *Nature Communications* **5** (2014), 10.1038/ncomms4782.
- Zhang, T., Li, X., and Gao, H., "Fracture of graphene: a review," *International Journal of Fracture* **196**, 1–31 (2015).

- Zhang, Z., Zhang, X., Wang, Y., Wang, Y., Zhang, Y., Xu, C., Zou, Z., Wu, Z., Xia, Y., Zhao, P., and Wang, H. T., "Crack propagation and fracture toughness of graphene probed by raman spectroscopy," *ACS Nano* **13**, 10327–10332 (2019).
- Zhao, H. and Aluru, N. R., "Temperature and strain-rate dependent fracture strength of graphene," *Journal of Applied Physics* **108**, 064321 (2010).
- Zhao, X., Mao, B., Liu, M., Cao, J., Haigh, S. J., Papageorgiou, D. G., Li, Z., and Young, R. J., "Controlling and monitoring crack propagation in monolayer graphene single crystals," *Advanced Functional Materials*, 2202373 (2022).
- Zhong, T., Li, J., and Zhang, K., "A molecular dynamics study of young's modulus of multilayer graphene," *Journal of Applied Physics* **125**, 175110 (2019).